Chinese Chemical Letters 33 (2022) 4385–4388

Contents lists available at ScienceDirect

Chinese Chemical Letters

journal homepage: www.elsevier.com/locate/cclet

Au nanoparticles loaded on hollow BiOCl microstructures boosting CO_2 photoreduction

Siwen Gong[a], Fei Rao[a], Weibin Zhang[b], Qadeer-Ul Hassan[a], Zhaoqing Liu[c], Jianzhi Gao[a], Jiangbo Lu[a], Mirabbos Hojamberdiev[d], Gangqiang Zhu[a,*]

[a] School of Physics and Information Technology, Shaanxi Normal University, Xi'an 710062, China
[b] School of Physics and Optoelectronic Engineering, Yangtze University, Jingzhou 434023, China
[c] School of Chemistry and Chemical Engineering, Institute of Clean Energy and Materials, Guangzhou University, Guangzhou 510006, China
[d] Institute of Chemistry, Technical University of Berlin, Berlin 10623, Germany

ARTICLE INFO

Article history:
Received 12 October 2021
Revised 5 November 2021
Accepted 15 December 2021
Available online 20 December 2021

Keywords:
BiOCl
Au nanoparticles
Oxygen vacancy
Ohmic contact
CO_2 photoreduction

ABSTRACT

The BiOCl (BOC) synthesized by the water bath heating method was treated with sodium borohydride ($NaBH_4$) to introduce oxygen vacancies (OVs). At the same time, Au nanoparticles were loaded to prepare a series of Au/BiOCl samples with different ratios. OVs and Au nanoparticles can promote the light absorption of host photocatalyst in the visible region. The calculated work function of BiOCl and Au can verify the existence of Ohmic contact between the interface of them, which is conducive to the separation of charge carriers. Through a series of photoelectric tests, it was verified experimentally that the separation of charge carriers is indeed enhanced. The high-energy hot electrons produced by Au under the surface plasmon resonance (SPR) effect can increase the counts of electrons to participate in the CO_2 reduction reaction. Especially for 1.0%-Au/BOC, the yields of CO can reach 43.16 μmol g^{-1} h^{-1}, which is 6.6 times more than that of BOC. Therefore, loading precious metal on semiconductors is an effective strategy to promote the photocatalytic performance of CO_2 reduction reactions.

Photocatalytic reduction of CO_2 needs a very negative reduction potential, which requires the photocatalyst to have a relatively negative conduction band (CB) position. Generally, semiconductor photocatalysts that meet this condition have a wide band gap, which is not conducive to the absorption of visible light [1,2]. Introducing defects and loading precious metals can be used as two important methods to solve this problem [3–8]. Due to its unique electronic structure, oxygen vacancies (OVs) will change the light absorption capacity and photogenerated carrier mobility of the semiconductor photocatalyst, thereby enhancing its performance [9]. The local electrons near the OVs can induce shallow donor levels below CB [10,11]. The donor levels caused by the suitable content of OVs can further hybridize with the CB, thereby changing the Fermi level of the semiconductor and the forbidden band width [12]. Meanwhile, this energy level also promotes the separation of charge carriers [13].

The surface plasmon resonance (SPR) effect makes noble metal nanoparticles capture partial visible light, and then produce high-energy hot electrons [14–17]. In this way, semiconductor loaded with noble metals can use these high-energy hot electrons to drive chemical reactions on their surfaces. Meanwhile, the metal-semiconductor heterojunction that forms Ohmic contacts facilitates the separation of charge carriers and promotes the progress of photocatalytic reactions [18,19]. Thus, it is very critical to select the appropriate semiconductor and precious metal for constructing nanocomposites. BiOCl (BOC) is a wide-gap photocatalytic material. The CB position of BOC is relatively negative, generally between −0.9 V ∼ −1.1 V (*vs.* SHE), which matches with the potential of reducing CO_2 to CO (−0.51 V *vs.* SHE) and CH_4 (−0.24 V *vs.* SHE) [20]. BOC has a valence band (VB) position of 1.7 V ∼ 1.8 V (*vs.* SHE), which has sufficient oxidation capacity to decompose water (0.82 V *vs.* SHE), providing protons for CO_2 reduction [21]. Therefore, BOC can meet the potential requirements of CO_2 reduction. Loading metal nanoparticles with a suitable Fermi level can be selected to form a heterojunction in Ohmic contact with BOC, thereby improving the light absorption ability and the separation ability of photogenerated charge carriers.

In this work, the presence of OVs and Au nanoparticles in BOC (OVs-Au/BOC) not only significantly enhances the visible light absorption capacity of the composite sample, but also

* Corresponding author.
E-mail address: zgq2006@snnu.edu.cn (G. Zhu).

https://doi.org/10.1016/j.cclet.2021.12.039
1001-8417/

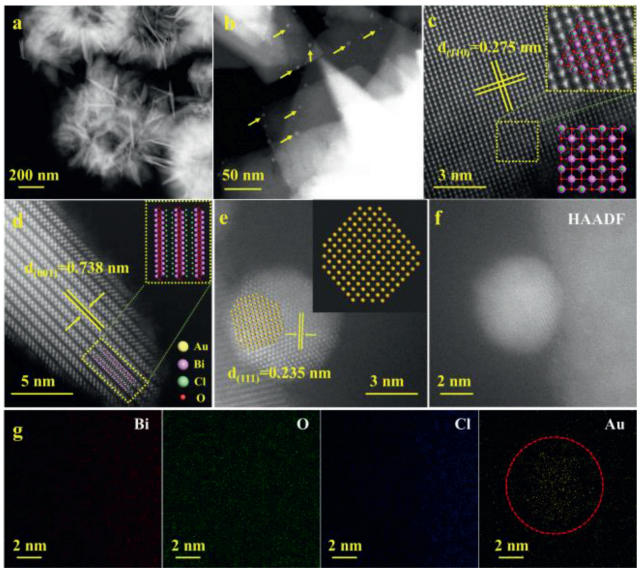

Fig. 1. The TEM images (a, b), HAADF-STEM images (c-e) and EDX mappings of 1.0%-Au/BOC (f, g).

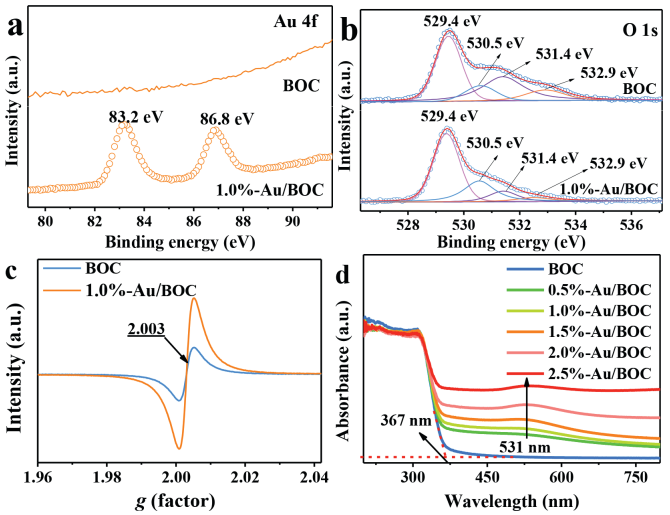

Fig. 2. The high-resolution XPS spectra of Au 4f (a), O 1s (b) and EPR spectra (c) of BOC and 1.0%-Au/BOC samples, UV–vis diffuse absorbance spectra of all prepared samples (d).

significantly improves the separation ability of photo-generated carriers, thereby greatly boosting the catalytic activity of the photocatalyst. Through the combination of experiments and DFT calculations, the improvement mechanism of photocatalytic activity and the reaction process of photocatalytic reduction of CO_2 are explored (Supplementary Notes 1–4 in Supporting information).

The synthesis process of BOC is described in Supplementary Note 5 (Supporting information). Furthermore, dissolve 0.2 g BOC in 30 mL deionized water, and then add the corresponding chloroauric acid solution and stirred for 1 h (Au:Bi molar ratios of 0.5%, 1.0%, 1.5%, 2.0%, 2.5%). Weigh an appropriate amount of $NaBH_4$ (the molar concentration is 5 times than the Au concentration in the corresponding mixed solution), dissolve it in 30 mL of deionized water, and quickly pour it into the stirred mixed solution. The precipitate was washed several times with deionized water and alcohol, and collected after drying for 6 h at 60 °C. According to the different proportions of Au loading, the photocatalyst is recorded as BOC, 0.5%-Au/BOC, 1.0%-Au/BOC, 1.5%-Au/BOC, 2.0%-Au/BOC, 2.5%-Au/BOC.

As shown in Fig. S1a (Supporting information), the X-ray diffraction (XRD) pattern is exactly the same as that of the tetragonal BiOCl (PDF #85–0861). However, the diffraction peaks of Au are not observed after because of the low loading counts and unique dispersion [19]. As shown in Fig. S1b (Supporting information), FTIR further confirms the phase structure of as-prepared samples. In BOC and Au/BOC samples, the peak at 527 cm^{-1} is attributed to the Bi-O stretching mode [19], and the peaks at 1293, 1423, and 1663 cm^{-1} are attributed to the N—H —O group, pyrrole and free C=O stretch mode [22]. There is no obvious change in the position of the signal indicates that further characterization methods are needed to observe the loaded Au species.

The TEM image of 1.0%-Au/BOC is shown in Fig. 1a, which maintains the flower-shaped appearance of hollow structure of BOC stacked of nanosheets, where some nanoparticles with a diameter of 5–6 nm are distributed on the surface (Fig. 1b). In the HAADF-STEM images (Figs. 1c and d), two clear lattice plane spacings of 0.275 nm and 0.738 nm are shown, corresponding to the (110) and (001) of BiOCl, respectively. Fig. 1e shows a set of clear lattice plane spacing 0.235 nm, corresponding to the (111) lattice plane of Au^0. Energy dispersive X-ray spectroscopy (EDS) further shows the distribution of elements. From Figs. 1f and g, it can be seen that the Bi, O, and Cl elements are uniformly distributed on the nanosheets, while the Au elements are mostly concentrated to form the nanoparticles. It proved that Au^0 was successfully loaded onto BiOCl nanosheets.

The element composition and chemical state of the sample were further analyzed by X-ray photoelectron spectroscopy (XPS). The survey spectra and high-resolution spectra of Bi 4f and Cl 2p of BOC and 1.0%-Au/BOC samples are shown in Fig. S2 (Supporting information). In the HR-XPS of Au 4f, the peaks at 83.2 eV and 86.8 eV can be attributed to Au^0 [23], indicating that Au exists in the composite sample in the form of metal, and there is no Au element in the pure BOC sample (Fig. 2a). In Fig. 2b, three peaks at 529.4, 531.4 and 532.9 eV are ascribed to lattice oxygen, surface adsorbed oxygen, and surface adsorbed oxygen in water molecules [24]. The O at 530.5 eV is OV. It can be seen that the peak area of OVs in the metal-loaded BOC has increased, which demonstrates that the amount of OVs has been increased. In order to directly prove the existence and variation of OVs in as-prepared samples, the electron paramagnetic resonance (EPR) spectroscopy of the sample was tested, as shown in Fig. 2c. BOC and 1.0%-Au/BOC both show resonance signals at $g = 2.003$ [25], while the signal of BOC is relatively weak. It indicates that OVs have existed in BOC. After chemical reduction, more OVs are generated, so the peak intensity in 1.0%-Au/BOC gets higher, which is consistent with the conclusion in XPS.

Fig. 2d records the UV–vis absorption spectra of BOC and Au/BOC, reflecting the light absorption properties of the photocatalysts. The location of the absorption band edge of BOC is about 367 nm, which shows that BOC has strong absorption for ultraviolet light and has a weak response to visible light. This weak visible light response can be attributed to the existence of the OVs in BOC. As the loading of Au nanoparticles increases, the absorption of the photocatalyst in the visible light region becomes more robust. In addition, an absorption peak that appears near 531 nm can be attributed to the SPR effect of Au nanoparticles [26]. From the absorption edge of as-prepared samples, it can be observed that the edge gradually redshifts toward the visible region with the increase of the Au loading, owing to the increasing content of OVs. OVs are mainly reflected in two aspects to promote the activity of semiconductor photocatalysts. Firstly, the localized electrons on OVs energy level can be excited to the CB under visible light [2]. Secondly, the intermediate energy levels of these defect states may

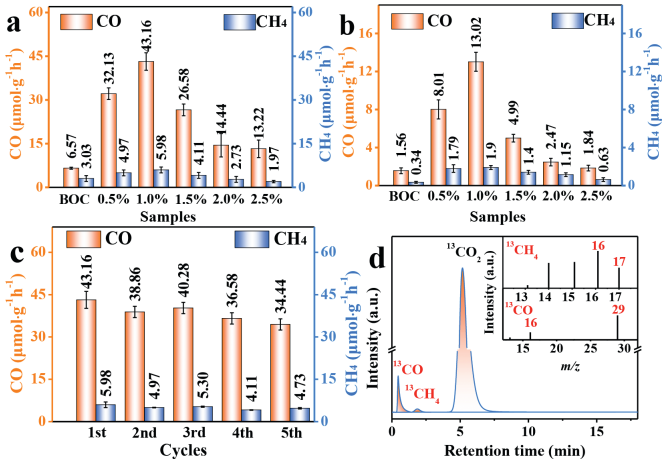

Fig. 3. Generation rate of CO and CH_4 under simulated sunlight (a), under visible light (b), cyclic experiment over 1.0%-Au/BOC (c), mass spectra of $^{13}CH_4$ (*m/z* 17) and ^{13}CO (*m/z* 29) generated over 1.0%-Au/BOC (d).

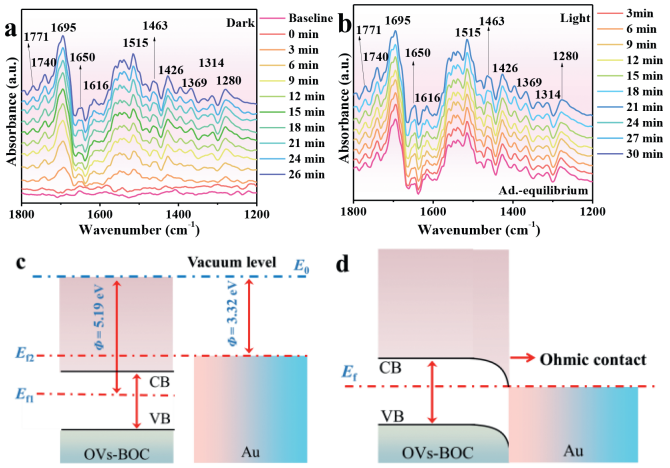

Fig. 4. The *in situ* FTIR spectra of 1.0%-Au/BOC during the CO_2 reduction process (a) in dark and (b) with illumination under simulated light, schematic diagram of energy band change of 1.0%-Au/BOC before (c) and after (d) contact (Φ is the work function, E_0 is the vacuum level, E_{f1} and E_{f2} are the Fermi levels of OVs-BOC and Au^0, respectively, and E_f is the Fermi level of 1.0%-Au/BOC).

also accept electrons in the valence band (VB) transition under the excitation of visible light, and indirectly transfer photoelectrons to CB, which not only broadens the visible light response range, but also inhibits the recombination of e^--h^+ pairs [27]. According to the DFT calculation of the density of states (DOS), the conclusion can be drawn that the shallow energy levels come into being by O 2p orbit in OVs-BOC (Fig. S3 in Supporting information), which is overlapped with the bottom of the CB to narrow the band gap, thereby enhancing light absorption.

The photocatalytic performance of the as-prepared samples is evaluated by the CO_2 photoreduction test. As shown in Fig. 3a, after 1 h of simulated sunlight exposure, the formation rate of CO and CH_4 over BOC are 6.57 μmol/g and 3.03 μmol/g, respectively. The loading of Au^0 in BOC and the introduction of OVs remarkably boosted the photoreduction activity of CO_2 (Table S1 in Supporting information). Especially for 1.0%-Au/BOC, the yields of CO and CH_4 can reach up to 43.16 μmol $g^{-1}h^{-1}$ and 5.98 μmol $g^{-1}h^{-1}$, respectively. The rate of CO generation is 6.6 times higher than that of pristine BOC. Furthermore, the activity of 1.0%-Au/BOC is still very good compared with other photocatalysts (Table S2 in Supporting information). However, with the continuous increase of the loading, the photocatalytic activity decreased, which is due to the size augment of Au^0 nanoparticles. The changes in the specific surface area (S_{BET}) and pore size distribution of the pure BOC sample and composite material can be observed through the nitrogen (N_2) adsorption-desorption curves (Fig. S4 in Supporting information), which is an essential factor affecting the photocatalytic activity. With reference to the IUPAC classification, the isotherm of the sample shows a typical IV-type isotherm and H3 hysteresis, indicating that the synthesized material has a mesoporous structure. After loading Au^0, the increased S_{BET} of the sample is beneficial to the photocatalytic performance. But as the loading ratios increase, the S_{BET} of the sample gradually decreases, which decreases the surface reaction and adsorption sites for the target gas. The size augment of Au^0 nanoparticles will cause the photogenerated electrons to recombine before reaching the surface of the Au^0 to react with CO_2, thereby reducing the reaction activity [20]. Therefore, it is extremely important to adjust the loading amount so that the Au^0 nanoparticles maintain the appropriate amount and size to promote the CO_2 photoreduction performance.

In order to verify that the promotion of the photocatalytic activity is due to the SPR effect of Au^0, the performance test under visible light irradiation was carried out. It can be observed that the photocatalytic performance trends of all samples are consistent with the results under simulated sunlight (Fig. 3b). After loading Au^0 nanoparticles, 1.0%-Au/BOC has the most significant increase. It can reach CO: 13.02 μmol $g^{-1}h^{-1}$, CH_4: 1.90 μmol $g^{-1}h^{-1}$, respectively, which is 8 times and 5 times than BOC. It can be proved that the loading of Au^0 nanoparticles enhances the effective absorption of visible light. Detailed performance data is shown in the supporting documents (Table S3 in Supporting information). In addition, a cyclic measurement was performed to manifest the stability of 1.0%-Au/BOC. Even after five photocatalytic reactions, 1.0%-Au/BOC still maintains high reactivity (Fig. 3c). By comparing the XRD before and after the reaction (Fig. S5a in Supporting information), it can be seen that the phase structure of the catalyst was not destroyed even after several photocatalytic reduction experiments of CO_2, which indicates that 1.0%-Au/BOC possesses high stability.

To explore the source of carbon in the product, a sequence of experiments have been done to prove that under the effect of the photocatalyst, CO_2 is reduced to other carbon-containing substances (Fig. S5b in Supporting information). In order to more intuitively verify the source of carbon in the product, the isotope labeling method ($^{13}CO_2$) was used in the experiment. From Fig. 3d, the peaks of 1.0%-Au/BOC at *m/z* 17 and *m/z* 29 can be ascribed to $^{13}CH_4$ and ^{13}CO, respectively, which proves the carbon in CH_4 and CO comes from the $^{13}CO_2$.

To explore the specific process of CO_2 reduction and the intermediate products, *in-situ* FT-IR tests were carried out in the presence or absence of light irradiation condition. As exhibited in Fig. 4a, the adsorption/desorption equilibrium is reached in the dark environment. The peaks at 1650 cm^{-1} correspond to H_2O, and the peaks at 1280 and 1369 cm^{-1} attributed to bicarbonate (HCO_3^-), the peaks at 1314, 1426, 1463, and 1616 cm^{-1} ascribed to carbonate (CO_3^{2-}), which are all caused by the initial reactive adsorption of CO_2 [28–30]. The peaks at 1515 and 1771 cm^{-1} correspond to formate ($HCOO^-$), and the peaks at 1695 and 1740 cm^{-1} correspond to CO_2^- and CO, respectively [12,19]. These are important intermediate products in the reduction of CO_2. After turning on the light, as shown in Fig. 4b, it can be observed that the shape of the *in-situ* infrared peak has no obvious change, but the intensity is significantly increased, especially for CO and $HCOO^-$. The increase of these two important intermediate products represents the rapid progress of the reaction. The specific reaction process is listed in Supplementary Note 6 (Supporting information).

After loading Au nanoparticles, the performance of the photocatalyst has been greatly improved. The adsorption of CO_2 over the surface of photocatalysts has an important influence on CO_2

photoreduction. The CO_2 adsorption curve has been shown in Fig. S6 (Supporting information). It can be found that there is no significant difference between the two samples, which indicates that in this experiment, the CO_2 physical adsorption ability is not the main factor impacting the photocatalytic performance. The enhancement of photocatalytic performance is governed by other factors.

Promoting the effective separation of photogenerated carriers is an important aspect to boost the activity of photocatalysts. Fig. S7 (Supporting information) shows the surface photovoltage spectra (SPV), the photocurrent response, the impedance spectroscopy (EIS) and the fluorescence spectra, which suggests that the Au^0 component can improve the separation ability and suppress the recombination of photogenerated carriers so that the activity of the photocatalyst has been improved.

The fundamental reason why the separation ability of photogenerated carriers has been improved will be further explored through DFT calculation. The heterojunction composed by metal nanoparticles and semiconductor is favorable for charge carrier transfer. As shown in Fig. S8 (Supporting information), the work function of OVs-BOC (110) (5.19 eV) is higher than the work function of Au^0 (111) (3.32 eV), so an Ohmic contact can be formed in the interface between them [15]. The band structure of Au^0 and OVs-BOC before contact is exhibited in Fig. 4c. After contact (Fig. 4d), the electrons of Au^0 flow to OVs-BOC to achieve a thermodynamic balance, thereby bending the energy band of OVs-BOC to form an Ohmic contact. When 1.0%-Au/BOC was excited by light with suitable energy, photogenerated electrons jumped from VB in OVs-BOC to CB. In addition, the photogenerated electrons move to Au^0 under the effect of the built-in electric field, which improves the separation ability of photogenerated electron-hole pairs.

In summary, the semiconductor is mainly excited by ultraviolet light to produce e^-/h^+ pairs in the BOC without modification; when OVs are present, OVs can form shallow energy levels near the CB, which can not only hybridize with the bottom of the CB to narrow the band gap, and can also be used as a step for photogenerated electrons. The electrons generated by light excitation can first jump to the OVs energy level and then jump to the CB. This process will absorb visible light, thereby enhancing the light absorption. After loading Au^0, the electrons on the CB will move to Au nanoparticles to participate in the reaction, enhancing the separation ability of e^-/h^+ pairs. In addition, Au nanoparticles will absorb visible light and produce the SPR effect and generate hot electrons. The hot electrons with higher energy will cross the contact barrier between the semiconductor and the metal and move to the CB of the semiconductor to participate in the reaction, so that the number of available electrons participating in the reaction will increase, which in turn accelerate the reaction rate. Our work provides a new perspective for the use of defects and metal loading to solve the problem of low efficiency of photoreduction of CO_2.

Declaration of competing interest

The authors declare that they have no known competing financial interests or personal relationships that could have appeared to influence the work reported in this paper.

Acknowledgments

This work was supported by the National Natural Science Foundation of China (Nos. 51772183, 52072230), and the Yulin Science and Technology Project (No. CXY-2020–040). The authors also thank Professor Jiangbo Lu, Dr. Wang Li, Dr. Hongmei Jing and Dr. Lujun Zhu for the help in using ac-TEM (the Electron Microscopy Platform of School of Physics and Information Technology, Shaanxi Normal University, Xi'an, China).

Supplementary materials

Supplementary material associated with this article can be found, in the online version, at doi:10.1016/j.cclet.2021.12.039.

References

[1] X. Liu, P. Wang, H. Zhai, et al., Appl. Catal. B: Environ. 232 (2018) 521–530.
[2] S. Cao, B. Shen, T. Tong, et al., Adv. Funct. Mater. 28 (2018) 1800136.
[3] P. Qiu, J. Wang, Z. Liang, et al., Chin. Chem. Lett. 32 (2021) 3501–3504.
[4] B. Sun, Z. Liang, Y. Qian, et al., ACS Appl. Mater. Inter. 12 (2020) 7257–7269.
[5] Z. Liang, Y. Xue, X. Wang, et al., Chem. Eng. J. 421 (2021) 130016.
[6] Y. Chen, S. Ji, W. Sun, et al., Angew. Chem. Int. Ed. 59 (2020) 1295–1301.
[7] S. Jian, Z. Tian, J. Hu, et al., Adv. Powd. Mater. 1 (2022) 100004.
[8] G. Zhao, W. Ma, X. Wang, et al., Adv. Powd. Mater. 1 (2022) 100008.
[9] J. Mizusaki, Solid State Ionics 52 (1992) 79–91.
[10] M. Xing, J. Zhang, F. Chen, et al., Chem. Commun. 47 (2011) 4947–4949.
[11] F. Zuo, L. Wang, T. Wu, et al., J. Am. Chem. Soc. 132 (2010) 11856–11857.
[12] X. Xiang, F. Pan, Y. Li, Adv. Compos. Hybrid Mater. 1 (2018) 6–31.
[13] F. Rao, G. Zhu, W. Zhang, et al., ACS Catal. 11 (2021) 7735–7749.
[14] N. Celebi, M.Y. Aydin, F. Soysal, et al., J. Alloy. Compd. 860 (2021) 157908.
[15] M. Sharma, G. Singh, R. Vaish, Nanotechnology 32 (2021) 145716.
[16] S. Liu, W. Qi, S. Adimi, et al., ACS Appl. Mater. Inter. 13 (2021) 7238–7247.
[17] R.B. Wei, P.Y. Kuang, H. Cheng, et al., ACS Sustain. Chem. Eng. 5 (2017) 4249–4257.
[18] F. Rao, G. Zhu, W. Zhang, et al., Appl. Catal. B: Environ. 281 (2021) 119481.
[19] S. Gong, G. Zhu, R. Wang, et al., Appl. Catal. B: Environ. 297 (2021) 120413.
[20] L. Fu, R. Wang, C. Zhao, et al., Chem. Eng. J. 414 (2021) 128857.
[21] J. Hu, W. Fan, W. Ye, et al., Appl. Catal. B: Environ. 158 (2014) 182–189.
[22] X. Li, W. Zhang, W. Cui, et al., Appl. Catal. B: Environ. 221 (2018) 482–489.
[23] J. Wan, Y. Zhang, R. Wang, et al., J Hazard. Mater. 384 (2020) 121484.
[24] X. Xie, Q.U. Hassan, H. Lu, et al., Chin. Chem. Lett. 32 (2021) 2038–2042.
[25] J. Nie, J. Gao, Q. Shen, et al., Sci. China Mater. 63 (2020) 2272–2280.
[26] Y. Tian, L. Ma, X. Tian, et al., Chemosphere 269 (2021) 128717.
[27] M. Humayun, L. Xu, L. Zhou, et al., Nano Res. 11 (2018) 6391–6404.
[28] J.Y. Tang, R.T. Guo, W.G. Pan, et al., Appl. Surf. Sci. 467 (2019) 206–212.
[29] W. Wu, K. Bhattacharyya, K. Gray, et al., J. Phys. Chem. C 117 (2013) 20643–20655.
[30] R.W. Stevens, Jr., R.V. Siriwardane, J. Logan, Energy Fuels 22 (2008) 3070–3079.